

**$^{63}\text{Cu}(n,\gamma)$  cross section measured via 25 keV activation and time of flight**

M. Weigand,<sup>1,\*</sup> C. Beinrucker,<sup>1</sup> A. Couture,<sup>2</sup> S. Fiebiger,<sup>1</sup> M. Fonseca,<sup>3,4</sup> K. Göbel,<sup>1</sup> M. Heftrich,<sup>1</sup> T. Heftrich,<sup>1</sup> M. Jandel,<sup>2</sup> F. Käppeler,<sup>5</sup> A. Krása,<sup>6</sup> C. Lederer,<sup>1,7</sup> H. Y. Lee,<sup>2</sup> R. Plag,<sup>1</sup> A. Plompen,<sup>6</sup> R. Reifarth,<sup>1</sup> S. Schmidt,<sup>1</sup> K. Sonnabend,<sup>1</sup> and J. L. Ullmann<sup>2</sup>

<sup>1</sup>Goethe University Frankfurt, Institute for Applied Physics, Max-von-Laue Str. 1, 60438 Frankfurt, Germany

<sup>2</sup>Los Alamos National Laboratory, Los Alamos, New Mexico, 87545, USA

<sup>3</sup>LIBPhys-UNL, DF, FCT, Universidade Nova de Lisboa, 2829-516 Caparica, Portugal

<sup>4</sup>Universidade Europeia, Laureate International Universities, Estrada da Correia 53, 1500-210 Lisboa

<sup>5</sup>Karlsruhe Institute of Technology, Campus Nord, Institut für Kernphysik, 76021 Karlsruhe, Germany

<sup>6</sup>EC-JRC, Retieseweg 111, B-2440 Geel, Belgium

<sup>7</sup>School of Physics and Astronomy, University of Edinburgh, Edinburgh EH9 3JZ, United Kingdom

(Received 20 October 2016; published 31 January 2017)

In the nuclear mass range  $A \approx 60$  to 90 of the solar abundance distribution the weak  $s$ -process component is the dominant contributor. In this scenario, which is related to massive stars, the overall neutron exposure is not sufficient for the  $s$  process to reach mass flow equilibrium. Hence, abundances and isotopic ratios are very sensitive to the neutron capture cross sections of single isotopes, and nucleosynthesis models need accurate experimental data. In this work we report on a new measurement of the  $^{63}\text{Cu}(n,\gamma)$  cross section for which the existing experimental data show large discrepancies. The  $^{63}\text{Cu}(n,\gamma)$  cross section at  $k_B T = 25$  keV was determined via activation with a quasistellar neutron spectrum at the Joint Research Centre (JRC) in Geel, and the energy dependence was determined with the time-of-flight technique and the calorimetric  $4\pi$  BaF<sub>2</sub> detector array DANCE at the Los Alamos National Laboratory. We provide new cross section data for the whole astrophysically relevant energy range.

DOI: [10.1103/PhysRevC.95.015808](https://doi.org/10.1103/PhysRevC.95.015808)

## I. INTRODUCTION

Nearly all of the observed abundances of heavy elements are either formed by the slow ( $s$ ) or the rapid ( $r$ ) neutron capture process in almost equal shares. The precise  $s$ -process path along the valley of stability, however, depends on temperatures and neutron densities in the relevant scenarios, cross sections, and half-lives in case of unstable isotopes. The  $s$  process is believed to occur in two astrophysical scenarios. One is the so-called *main*  $s$ -process component in evolved thermally pulsating low-mass stars in the asymptotic giant branch. The second scenario is that of massive stars, where the *weak*  $s$ -process component occurs when these stars reach the He-core burning phase and later the convective C-shell burning phase. During these periods, the  $^{22}\text{Ne}(\alpha,n)^{25}\text{Mg}$  reaction provides neutron densities of around  $10^6$  cm<sup>-3</sup> at  $3 \times 10^8$  K and  $10^{12}$  cm<sup>-3</sup> at  $1 \times 10^9$  K, respectively [1,2].

In contrast to the main component, the overall neutron exposure is much lower for the weak component. Consequently, mass flow equilibrium is not reached in contrast to the main component, where  $\langle\sigma\rangle_{kT} N_s \approx \text{const}$  is observed between the mass numbers of closed neutron shells [3].  $N_s$  is the  $s$ -process abundance of the species and  $\langle\sigma\rangle_{kT} := \langle\sigma v\rangle/v_T$

is its Maxwellian-averaged cross section, where  $v_T$  denotes the mean thermal velocity. This means the cross sections of single isotopes have an impact on the production yield of the next-nearest neighbors in the mass flow direction. Regarding the solar abundance pattern, the weak  $s$  process is the major contributor in the mass range of  $A \approx 60$  to 90. The sensitivity of the nucleosynthesis yield to the cross sections of the copper isotopes has been shown in [4]. This implies that, among others, the copper isotopes are important for the nucleosynthesis models of the weak  $s$  process, but not exclusively. Since the abundance pattern of the  $r$  process can be obtained by subtracting the expected  $s$ -process pattern from the observed solar abundances, new neutron capture cross section data also have an impact on  $r$ -process models [5].

The focus of this work lies on  $^{63}\text{Cu}$ , which is just in the transition region between nucleosynthesis dominated by nuclear statistical equilibrium (NSE) during the final stage of massive stars and by the weak  $s$  process. Figure 1 shows the area around  $^{63}\text{Cu}$  in the chart of nuclei. Capture on  $^{63}\text{Cu}$  produces the unstable  $^{64}\text{Cu}$ , which decays, with a half-life of 12.7 h, either via  $\beta^-$  to  $^{64}\text{Zn}$  or via  $\beta^+$  to  $^{64}\text{Ni}$  [6].  $^{64}\text{Ni}$  shields  $^{64}\text{Zn}$  from the contributions of the  $r$  process. The dominant producer of  $^{64}\text{Zn}$  is the NSE, but [7] still gives a 14% contribution by the weak  $s$  process.

There have been several experimental efforts to measure the  $^{63}\text{Cu}(n,\gamma)$  cross section, but there are discrepancies between the experimental data [4,8]. Therefore, a new activation experiment at the Joint Research Centre (JRC) in Geel, Belgium has been performed to determine the cross section with a quasithermal neutron spectrum at  $k_B T = 25$  keV, presented in Sec. II. Furthermore, in order to determine the energy-

\* m.weigand@gsi.de

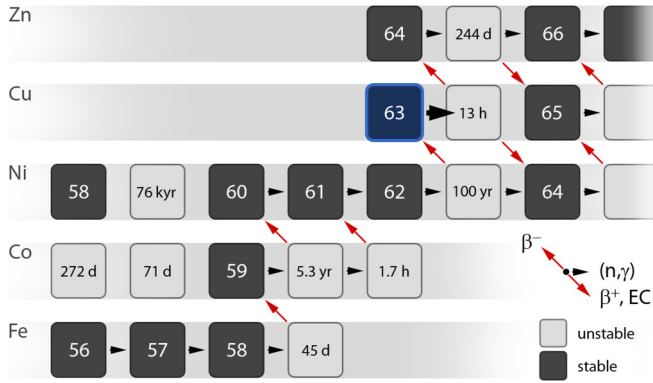


FIG. 1. The  $s$ -process path in the iron-zinc-region. Following neutron capture on  $^{63}\text{Cu}$ , the product  $^{64}\text{Cu}$  decays according to [6] with a half-life of 12.7 hours either to  $^{64}\text{Ni}$  or to  $^{64}\text{Zn}$ .

dependent neutron-capture cross section and to extend the data range to the full astrophysically interesting energy region from  $k_B T = 1$  to 100 keV, an experiment at the Los Alamos National Laboratory was conducted using the time-of-flight technique and the calorimetric  $4\pi$  BaF<sub>2</sub> detector array DANCE (Detector for Advanced Neutron Capture Experiments) [9]. This experiment and the corresponding analysis are described in Sec. III. The final Sec. IV discusses the experimental results.

## II. THE ACTIVATION EXPERIMENT

The activation of  $^{63}\text{Cu}$  was performed at the European Commission Joint Research Centre (EC-JRC) in Geel, Belgium. Providing a quasistellar neutron spectrum, the activation technique has proved to be a suitable method for the determination of Maxwellian averaged cross sections (MACS) at  $k_B T = 25$  keV [10]. The neutrons were produced with protons impinging on a lithium target using the  $^7\text{Li}(p,n)^7\text{Be}$  reaction whose threshold lies at 1881 keV. The proton beam for the experiment was provided by a 7 MV Van de Graaff accelerator and the proton energy was tuned to  $E_p = (1912 \pm 2)$  keV. The metallic Li material was evaporated onto silver backings with a thickness of  $27.5 \mu\text{m}$ . During operation the neutron production targets were water cooled to dissipate the heat load.

### A. Samples and irradiation

Two circular samples 12 mm in diameter were cut from a 0.2 mm thick foil of natural copper with a  $^{63}\text{Cu}$  content of 69.15%. Gold foils were used in a gold-copper-gold sandwich configuration in order to determine the integrated neutron flux  $\Phi_n$  at the sample position using the well known gold cross section. The gold monitors had the same diameter as the copper samples and a thickness of 0.3 mm. The sample stacks were placed just behind the neutron production target to ensure a complete coverage of the emitted neutrons and were irradiated for about one half-life of  $^{64}\text{Cu}$ . Further information on the samples and the irradiation times  $t_i$  are collected in Table I.

TABLE I. The number of nuclei in the respective sample  $^A N$ , irradiation times  $t_i$ , correction factors  $f_b$ , and time integrated neutron fluxes  $\Phi_n$ .

Act.	Sample	$^A N$ ( $\times 10^{20}$ )	$t_i$ (s)	$f_b$	$\Phi_n$ ( $\times 10^{-15} \text{ mb}^{-1}$ )
1	Cu I	11.8	51046	0.7048	1.39
1	Au Ia	1.84		0.9291	
1	Au Ib	1.87		0.9291	
2	Cu II	11.9	55119	0.6949	4.06
2	Au IIa	3.31		0.9271	
2	Au IIb	3.25		0.9271	

### B. Neutron spectrum and flux

The shape of the neutron spectrum was estimated by simulations with the program PINO (proton in, neutron out) which utilizes the Monte Carlo method [11]. PINO considers the geometry of the Li layer, energy loss in the lithium layer, the sample position, and uncertainties in the proton energy. The simulated spectrum shown in Fig. 2 is in good agreement with a spectrum corresponding to a stellar Maxwell-Boltzmann distribution for the major part of the energy range, but with a cutoff at the high energy end. This has to be taken into account when calculating the 25 keV MACS for astrophysical scenarios.

The integrated fluxes applied for two copper samples are also given in Table I. The neutron fluxes of the two activation runs differ due the performances of the accelerator and the Li targets. The gold cross section of 683 mb at 25 keV published in [12] was used as reference for normalization.

Especially for short-lived isotopes the decay during the irradiation has to be considered with a correction factor  $f_b$ . Since the neutron flux may also fluctuate, its variability was continuously monitored at three-minute intervals by means of a BF<sub>4</sub> filled ionization chamber via the  $^{10}\text{B}(n,\alpha)^7\text{Li}$  reaction. The correction factors for both copper samples and gold

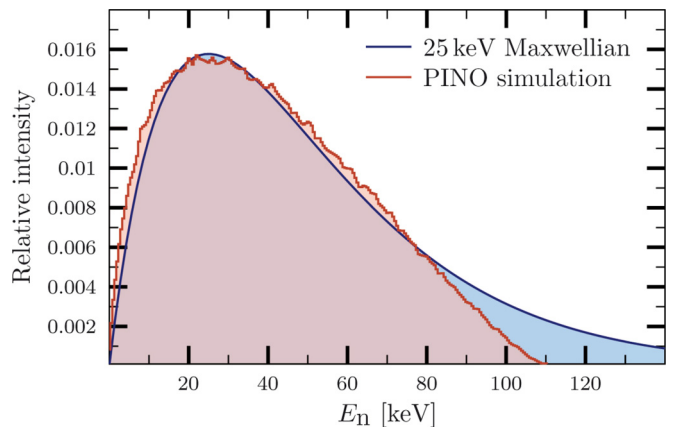


FIG. 2. A PINO simulation of the 25 keV neutron spectrum used for the activation (red) compared with the corresponding Maxwell-Boltzmann distribution (blue); see text for details.

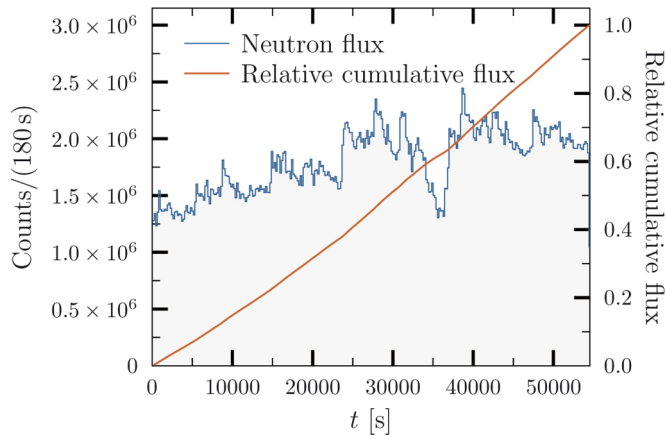


FIG. 3. The time dependence of the neutron flux for the second activation (blue) and the corresponding growth curve (red).

monitors were calculated via

$$f_b = \frac{\sum_i \Phi_i \exp[-\lambda(t_a - i \Delta t)]}{\sum_i \Phi_i}, \quad (1)$$

with the neutron detector counts  $\Phi_i$  for each time interval  $i \Delta t$ , the duration of the activation  $t_a$ , and the decay constant  $\lambda$  of the activation product. Figure 3 shows the time development of the neutron flux for the second activation run illustrating that the corresponding growth curve is rather smooth. The resulting correction factors for both irradiations, compiled in Table I, are therefore very close to the constant flux case.

### C. Activity determination via $\gamma$ spectroscopy

After the activation of a sample with  $^A N$  nuclei, an averaged capture cross section  $\sigma$ , and a neutron flux  $\Phi$ , the total number of product nuclei  $^{A+1} N$  is

$$^{A+1} N = ^A N \Phi \sigma f_b. \quad (2)$$

The number of  $^{64}\text{Cu}$  nuclei was determined via  $\gamma$  spectroscopy with a high-purity germanium (HPGe) detector by analyzing the characteristic  $\gamma$  lines listed in Table II. Figure 4 shows an example spectrum from activation 1 to illustrate the low  $\gamma$ -ray background. The number of produced nuclei was then determined by the observed activity of the sample material as

$$^{A+1} N = \frac{C_\gamma}{I_\gamma \epsilon_\gamma f_b f_w f_{dt} f_{casc} \kappa_\gamma}, \quad (3)$$

TABLE II. Decay data for the relevant  $\gamma$  lines and the corresponding detection efficiencies  $\epsilon_\gamma$  of the used HPGe detector. Values for  $t_{1/2}$ ,  $E_\gamma$ , and  $I_\gamma$  were obtained from [13] and [14].

Isotope	$^{64}\text{Cu}$	$^{198}\text{Au}$
$t_{1/2}$	$(12.701 \pm 0.002)$ h	$(2.6947 \pm 0.0003)$ d
$E_\gamma$	1345.77 keV	411.80 keV
$I_\gamma$	$(0.475 \pm 0.011)\%$	$(95.62 \pm 0.06)\%$
$\epsilon_\gamma$	4.57%	10.8%

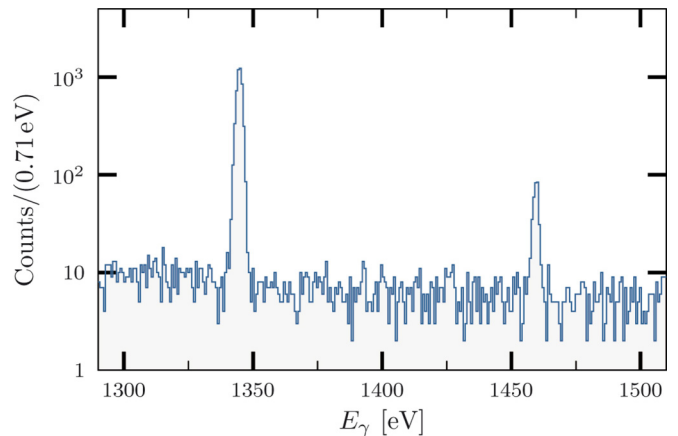


FIG. 4. Result of the  $\gamma$  counting after the first activation run. The  $\gamma$  line at the left at 1345.77 keV originates from the decay of  $^{63}\text{Cu}$ ; the line at 1460 keV is background from  $^{40}\text{K}$ .

with the intensity of the observed  $\gamma$  line  $I_\gamma$  and the  $\gamma$ -detection efficiency  $\epsilon_\gamma$ . Furthermore, correction factors for the decay during the waiting time between the irradiation and the  $\gamma$  counting and during the measurement ( $f_w$ ), as well as for detector deadtime ( $f_{dt}$ ) and self-absorption ( $\kappa_\gamma$ ), are necessary. The latter takes into account that  $\gamma$  rays may be absorbed on their way to the detector by the sample material itself. This effect was investigated with GEANT4 simulations and found to be in the order of 0.6%. Additionally, the effect of  $\gamma$  cascades during the decay of a nucleus was considered. Its strength depends on the distance between detector and sample. Hence, the corresponding correction factor  $f_{casc}$  was also estimated by means of GEANT4 simulations of the counting geometry. For  $^{64}\text{Cu}$  no cascade corrections are necessary, since it does not emit cascades.  $^{198}\text{Au}$  on the other hand decays via a  $\gamma$  cascade with a probability of 0.985%. However, the result from the simulations is that the effect of the  $\gamma$  cascade on the evaluated count numbers is only 0.46%.

### D. Uncertainties

The uncertainties of the determined cross sections arise from the counting of both the copper samples and the gold monitors. Statistical uncertainties amount to about 1.3%, while the systematic uncertainties dominate with 6.9% in total. The main sources for the systematic uncertainties are the  $\gamma$  intensity of the 1345.77 keV line of  $^{64}\text{Cu}$  with 2.32% and the detector efficiency with 3.9%. Furthermore, the determination of the neutron flux contributes 3.3% in total due to the uncertainty of the gold cross section of 1.2% and the observed variations between the monitors. All sources for systematic uncertainties are compiled in Table III.

### E. Cross sections

As previously shown, the neutron energy distribution of the activation experiment differs from an ideal Maxwellian distribution corresponding to a thermal energy of 25 keV. Hence, the activation experiment did not directly result in a cross section that is ready to use in nucleosynthesis

TABLE III. All sources for systematic uncertainties.

Source of uncertainty	Uncertainty (%)
Number of sample nuclei $^A N$	<0.1
Half-life $t_{1/2}$	<0.1
Gamma intensity $I_\gamma$	2.3
Detection efficiency $\epsilon_\gamma$	3.9
Detector deadtime $f_{dt}$	0.6
Factors $f_w$ and $f_b$	<0.1
Self-absorption $\kappa_\gamma$	0.3
Cascade correction $f_{casc}$	<0.1
Integrated neutron flux $\Phi_n$	3.3
Total systematic uncertainty	6.1

calculations, but has to be corrected for this difference. This correction can only be determined accurately if the energy dependence of the cross section is known, since resonances can have a significant influence. So, the needed correction factor  $f_{\text{stellar}}$  was based on the time-of-flight measurement presented in Sec. III. The time-of-flight (TOF) data were folded with both a 25 keV Maxwellian distribution and the PINO spectrum. The ratio of both results is the correction factor

$$f_{\text{stellar}} = \frac{\langle \sigma \rangle_{\text{TOF}, 25 \text{ keV}}}{\langle \sigma \rangle_{\text{TOF}, \text{PINO}}} = 1.053. \quad (4)$$

The new experimental cross sections are collected in Table IV. A discussion of the results follows in Sec. IV.

### III. THE TIME-OF-FLIGHT EXPERIMENT

The  $^{63}\text{Cu}$  time-of-flight experiment was performed at flight path 14 (FP14) at the Manuel Lujan Jr. Neutron Scattering Center at the Los Alamos Neutron Science Center (LANSCE). The facility offers a white spallation neutron source with a tungsten production target, driven by a 100  $\mu\text{A}$  pulsed proton beam at a repetition rate of 20 Hz. The isotopically enriched sample material consisted of  $(99.88 \pm 0.02\%)$   $^{63}\text{Cu}$  and was placed in the center of the DANCE array.

#### A. The DANCE array

The prompt  $\gamma$  rays following  $^{63}\text{Cu}(n, \gamma)$  capture events were detected with DANCE, a high efficiency scintillation detector suitable for measuring  $\gamma$  cascades. The array consists of 160  $\text{BaF}_2$  crystals arranged in spherical geometry (Fig. 5) that covers a solid angle of  $\Omega = 3.6\pi$ . The detector array is able to operate in calorimetric mode [15]. The full geometry would contain 162 crystals, but for practical reasons two have to

TABLE IV. Activation cross sections.

Cross section activation 1 <sup>a</sup>	$85.2 \pm 1.3 \pm 5.9 \text{ mb}$
Cross section activation 2	$88.6 \pm 0.9 \pm 6.1 \text{ mb}$
Weighted averaged $\langle \sigma \rangle_{\text{act}}$	$87.5 \pm 1.1 \pm 6.0 \text{ mb}$
Correction factor $f_{\text{stellar}}$	1.053
Stellar cross section $\langle \sigma \rangle_{25 \text{ keV}}$	$92.1 \pm 1.2 \pm 6.4 \text{ mb}$

<sup>a</sup>Uncertainties are statistical and systematic, respectively.

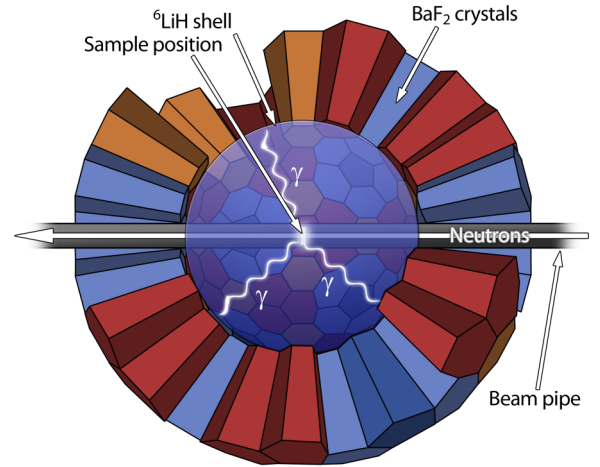


FIG. 5. A sketch of the DANCE array. Almost half of the crystals are blended out to give an insight. Colors distinguish between different crystal shapes; the blue disk indicates the neutron absorber.

be left out for the beam pipe. The inner and outer radii of the  $\text{BaF}_2$  sphere are 17 and 32 cm, respectively. The space between the beam pipe and the crystals is filled with a  $^6\text{LiH}$  spherical shell, which significantly reduces the background induced from scattered neutrons. This is very important, since capture cross sections are usually smaller than scattering cross sections [9]. The remaining background must be subtracted in the process of the data analysis.

All detected capture events possess certain properties used for analysis:

- (1) Neutron energy  $E_n$ , measured by the time-of-flight (TOF) method. The flight path length at DANCE is 20.29 m.
- (2) The energy  $E_\gamma$  deposited in a single crystal.
- (3) Summing over all  $E_\gamma$  of a measured event defined by a coincidence time window delivers the total  $\gamma$  energy  $E_{\text{tot}}$ .
- (4) Crystal multiplicity ( $M_{\text{cr}}$ ): Number of scintillator modules that have detected the event.
- (5) Cluster multiplicity ( $M_{\text{cl}}$ ): Number of scintillator groups, that have responded to the event. Here, neighboring crystals are combined to clusters. The energy of one  $\gamma$  ray is not always completely deposited in one crystal, but surrounding detector modules may also respond due to Compton scattering. Hence, the cluster multiplicity is closer to the real number of  $\gamma$  rays of a cascade and is therefore used for analysis [16,17].

A more detailed description of the DANCE array and the data acquisition is given in [18].

#### B. Neutron flux at DANCE

Data on the neutron energy distribution at DANCE are a necessity in order to be able to determine the energy dependence of a capture cross section. A detector dedicated to monitoring the neutron flux simultaneously to the experiment is positioned about two meters downstream from the center of the DANCE array. The device uses the  $^6\text{Li}(n, t)\alpha$  reaction

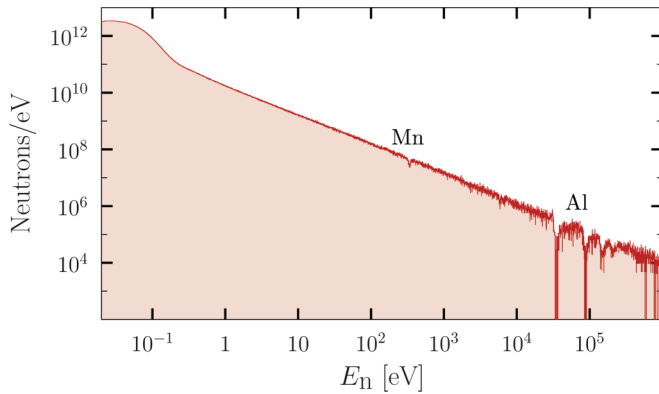


FIG. 6. The number of neutrons per eV plotted against the neutron energy. The neutron energy distribution at DANCE is continuously monitored with a  $^6\text{Li}$  detector. The origins of the absorption features at 500 eV and above 20 keV are neutron captures on beam line components and belong to Mn and Al, respectively.

for neutron detection via the energy deposited by the emitted particles. A resulting spectrum is shown in Fig. 6. The largest part of the spectrum, the range from 1 eV to 1 MeV, can be characterized by a  $E^{-1}$  power law. The low-energy end features a maximum, which is produced by a water moderator, which is the last interacting point of the neutrons inside the complex Lujan target before entering FP-14 [19]. The actual spallation target is a block of tungsten not in the direct line of sight from the sample. The absorption structures at  $E_n \approx 500$  eV and  $E_n > 20$  keV are caused by beam-line components and originate from neutron scattering on Mn and Al, respectively.

### C. Spectral analysis

The two-dimensional spectrum in Fig. 7 was used to investigate the effect of contaminants. As the spectral analysis based on the  $Q$  values and the observed resonances showed, there was no significant contamination in the sample material that could have produced background. Hence, the data had to be corrected only for ambient background and sample-induced neutron scattering.

### D. Sample-independent background

The main source for sample-independent background is natural radioactivity in the  $\text{BaF}_2$  crystals, originating from the Ra decay chain. Emitted  $\alpha$  particles can be discriminated because their scintillation light curve characteristically differs from those from  $\gamma$  rays. Additional  $\beta$  activity can easily be discriminated via the total energy  $E_{\text{tot}}$  deposited during the event, since the  $Q$  values are less than 3 MeV, which is low compared to the typical  $(n,\gamma)$   $Q$  values of 6 to 10 MeV. Applying a cut on  $M_{\text{cl}}$  was also used to discriminate background events, which appear at low multiplicities. So, only  $M_{\text{cl}} > 2$  events were used for further analysis. The remaining sample-independent background was corrected with data collected with an empty target holder. The resulting normalized background spectrum is shown in Fig. 8(b).

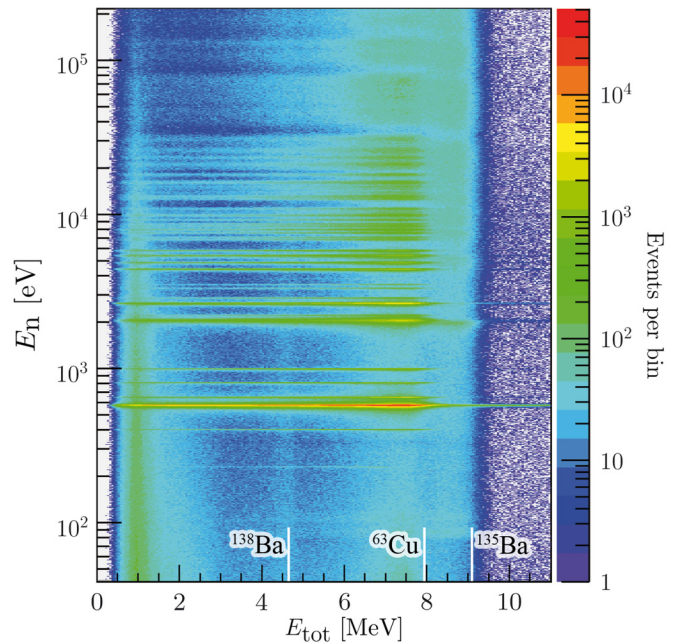


FIG. 7. A two-dimensional map of all detected capture events with  $E_n$  on the y axis and  $E_{\text{tot}}$  on the x axis. Neutron capture resonances appear as horizontal stripes. For the most prominent resonances pile-up effects are visible to the right, but can be neglected, since only relatively low count numbers are reached. The  $Q$  values of  $^{63}\text{Cu}$  (7.92 MeV) and the two most prominent barium isotopes,  $^{138}\text{Ba}$  (4.72 MeV) and  $^{135}\text{Ba}$  (9.11 MeV), are indicated.

### E. Sample-induced background

Since no other isotopes could be identified in the spectral analysis, the sample-induced background originates only from neutrons scattered at the sample. Eventually, the scattered neutrons reach the scintillator crystals and about 10% get captured in the detector material. Therefore, its spectral structure is determined by the neutron capture cross sections of the barium isotopes and their relative abundances in the crystals. For each neutron energy the contributions to the sum-energy distribution from the barium isotopes have specific ratios.

To investigate this background a 94 mg sample of  $^{208}\text{Pb}$  was chosen for several reasons. First, the low  $Q$  value for the neutron capture on  $^{208}\text{Pb}$  of only 3.94 MeV allows a clear separation of  $^{208}\text{Pb}(n,\gamma)$  from scatter events in the  $E_{\text{tot}}$  regime of  $^{63}\text{Cu}(n,\gamma)$ . Additionally, the ratio of neutron capture to neutron scattering is beneficial. For the whole considered energy range the capture cross section of  $^{208}\text{Pb}$  is at least two orders of magnitude smaller than its scattering cross section.

Of all barium isotopes  $^{135}\text{Ba}$  has the highest  $Q$  value of 9.11 MeV, which is even higher than the  $Q$  value of the  $^{63}\text{Cu}(n,\gamma)$  reaction of 7.9 MeV. Hence, above  $\approx 8.7$  MeV only capture events on  $^{135}\text{Ba}$  are visible. This was used to normalize and finally subtract the scattering background from the  $^{63}\text{Cu}$  data. The normalization factor  $\alpha_{\text{pb}}$  was calculated for each neutron energy bin with the integrated count numbers in

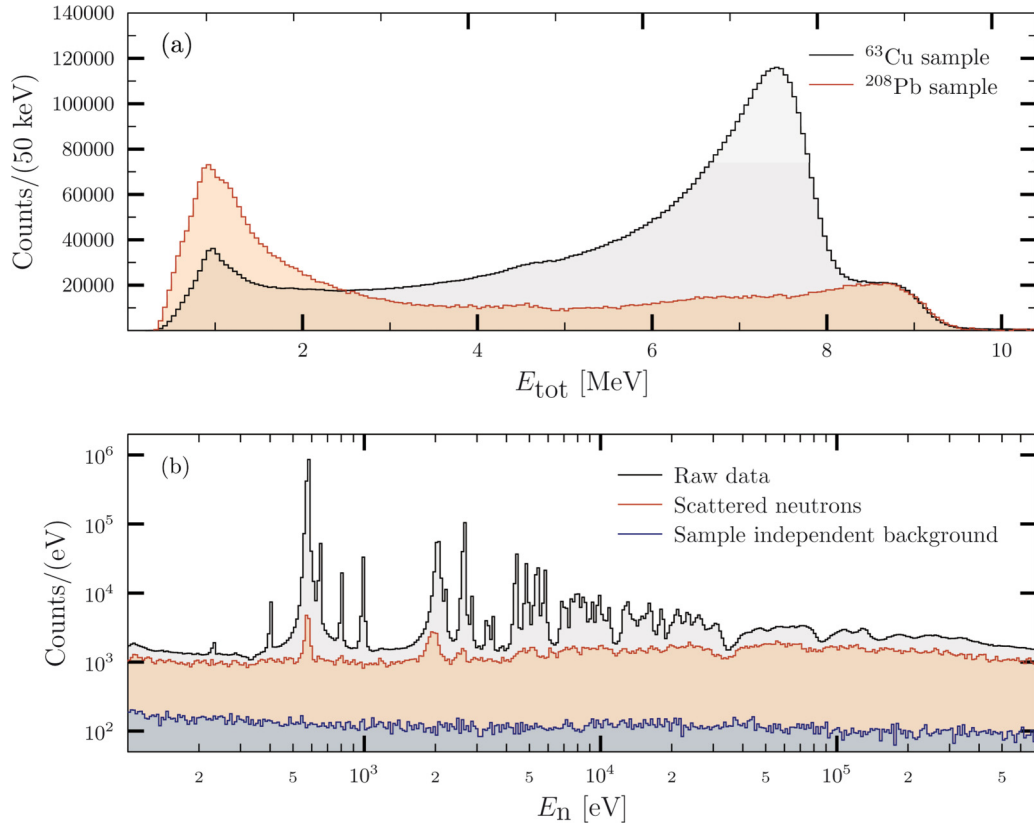


FIG. 8. (a) Total  $\gamma$ -energy spectrum measured with  $^{63}\text{Cu}$  (black) and  $^{208}\text{Pb}$  (red) for  $E_n = 588 \pm 50$  eV. The energy range from  $E_{\text{tot}} = 8.3$  to 9.2 MeV was used to normalize the background data for subtraction. The capture events between  $E_{\text{tot}} = 5.5$  and 8.3 MeV were considered for the cross section. (b) Total numbers of events as a function of the neutron energy (black) and the normalized background spectra for subtraction, acquired with an empty target holder (blue) and with the lead sample (red). The binning is logarithmic with 50 bins per decade.

the  $Q$ -value area of  $^{135}\text{Ba}$ :

$$\alpha_{\text{Pb}}(E_n) = \frac{\int_{8.3 \text{ MeV}}^{9.2 \text{ MeV}} C_{\text{Cu}}(E_{\text{tot}}, E_n) dE_{\text{tot}}}{\int_{8.3 \text{ MeV}}^{9.2 \text{ MeV}} C_{\text{Pb}}(E_{\text{tot}}, E_n) dE_{\text{tot}}}. \quad (5)$$

Figure 8(a) shows the sum energy spectrum for the 588 eV  $^{63}\text{Cu}(n, \gamma)$  resonance, where the sum energy peak of  $^{63}\text{Cu}$  is very prominent. For comparison the normalized data from the lead measurement are superimposed. At  $E_{\text{tot}} < 4.5$  MeV  $\gamma$  rays from the spallation source and scattered on the sample material produce a significant background. Since the scattering of  $\gamma$  rays depends on the nuclear charge, it is much stronger for the lead sample [9]. Therefore, only data above  $E_{\text{tot}} = 4.5$  MeV were used. The upper limit was set to  $E_{\text{tot}} = 7.9$  MeV. The resulting copper and background spectra are shown in Fig. 8(b).

### E. Normalization of the cross sections

The DANCE data were normalized with the new activation cross section presented in Sec. II. The normalization factor was obtained by numerical integration of the background-corrected capture yield weighted with the 25 keV PINO spectrum. The result is shown in Fig. 9(a) along with the evaluated data from TENDL-2015, plotted with the same binning for comparison.

### G. Uncertainties

The uncertainties of the differential cross section originate from the activation cross section used for the normalization, 3% uncertainty in the  $^6\text{Li}(n, t)\alpha$  cross section the flux determination is based on, and from the correction of the scattering background. The quality of the background correction depends on the normalization and therefore on an accurate  $\gamma$ -energy calibration to ensure an optimal match of the total  $\gamma$ -energy spectra in all used data sets. Based on the observed variations of  $\pm 0.016$  MeV in the energy calibration, the systematic uncertainty of the background correction was estimated to 4%. The total systematic uncertainty of the cross section therefore amounts to only 8.1%. The statistical uncertainties for single-neutron energy bins are typically in the order of 10%.

### H. Maxwellian averaged cross section

The cross sections measured with DANCE were converted into MACS via numerical integration, ready to use for nucleosynthesis calculations. We provide MACS for thermal energies from  $k_B T = 5$  to 100 keV. Due to the integration the statistical uncertainties of the differential cross sections have only a small effect. Hence, the systematic uncertainties dominate the MACS. For selected temperatures the data are

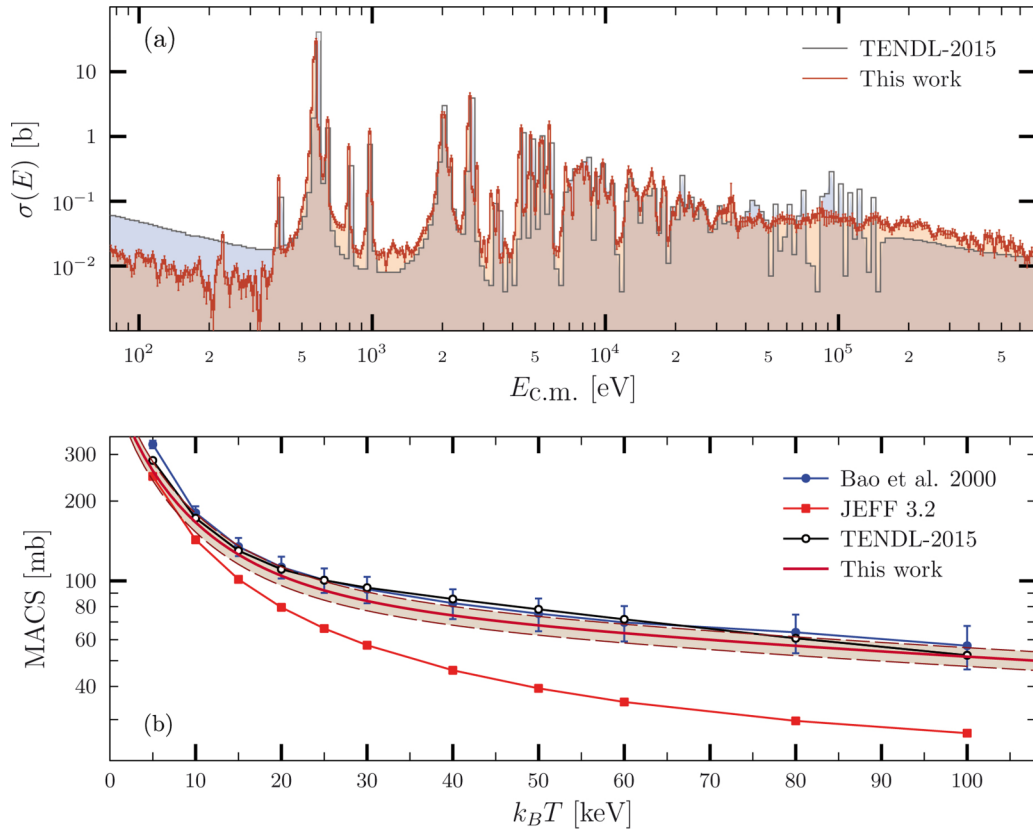


FIG. 9. (a) The measured neutron capture cross section of  $^{63}\text{Cu}$  as a function of neutron energy in comparison to the evaluated data from TENDL-2015. The binning is logarithmic with 50 bins per decade in both cases. (b) The MACS data are shown as a red line and the uncertainties are depicted as a grey area. For comparison, data from [20] and JEFF 3.2 are plotted as well.

also compiled in Table V, together with stellar reaction rates calculated via

$$r = \sigma_{\text{MACS}} N_A \alpha_{\text{SEF}} \sqrt{2E_{\text{kin}}/m_n}, \quad (6)$$

with the Avogadro number  $N_A$ , the kinetic energy  $E_{\text{kin}}$ , the neutron mass  $m_n$ , and the measured MACS  $\sigma_{\text{MACS}}$ .  $\alpha_{\text{SEF}}$

denotes the stellar enhancement factor which is for  $^{63}\text{Cu}$  equal 1.0 in the considered range [20].

#### IV. DISCUSSION

With our TOF data we confirm the temperature dependencies of the MACS that were calculated by Beer *et al.*

TABLE V. Maxwellian-averaged cross sections with statistical and systematical uncertainties, and stellar reaction rates in comparison to the KADoNiS database [21].

$k_B T$ (keV)	KADoNiS v0.3		This work	
	MACS (mb)	MACS $\pm$ stat $\pm$ sys (mb)	MACS $\pm$ stat $\pm$ sys (mb)	Rate ( $10^7 \text{ cm}^3 \text{ mol}^{-1} \text{ s}^{-1}$ )
5	198.0		$260.3 \pm 3.4 \pm 20.9$	1.53
10	109.0		$166.3 \pm 2.2 \pm 13.3$	1.38
15	80.4		$125.7 \pm 1.9 \pm 10.1$	1.28
20	67.4		$104.6 \pm 1.4 \pm 8.4$	1.23
25	60.3		$92.1 \pm 1.2 \pm 7.4$	1.21
30	55.7		$84.0 \pm 1.1 \pm 6.7$	1.21
40	49.1		$74.1 \pm 1.0 \pm 5.9$	1.23
50	46.7		$68.0 \pm 0.9 \pm 5.5$	1.27
60	44.9		$63.5 \pm 0.8 \pm 5.1$	1.30
80	39.0		$56.9 \pm 0.7 \pm 4.6$	1.34
100	34.3		$51.8 \pm 0.7 \pm 4.2$	1.36

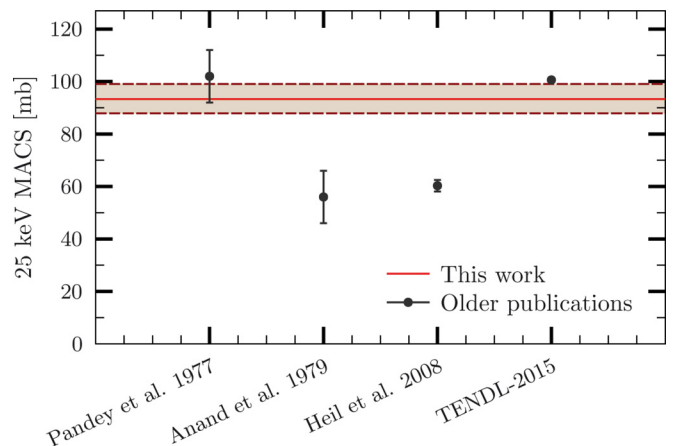


FIG. 10. Comparison of our 25 keV cross section with data from older publications. The MACS from Pandey *et al.* (1977) [8] were calculated by Bao *et al.* (2000) [20].

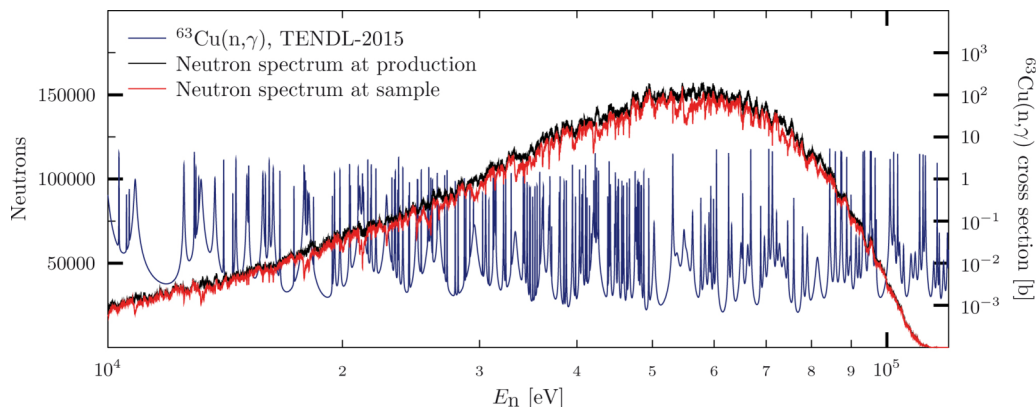


FIG. 11. Influence of a 1 mm copper backing on the neutron spectrum at the sample position (red) showing a pronounced self-shielding effect. For this calculation cross section data from TENDL-2015 was used, which is plotted in blue.

(1992) [22] and Bao *et al.* (2000) [20], both based on the data from Pandey *et al.* (1977) [8]. Most evaluated data libraries like JEFF 3.2 or JENDL 4.0, however, show a steeper decline of the MACS towards higher temperatures. There is good agreement between our data and TENDL-2015 which is plotted in Fig. 9 for comparison.

Figure 10 gives an overview over the experimental 25 keV MACSs of the last 40 years. There is large scatter among the data. Anand *et al.* in 1979 used the filtered reactor beam method, which only covered a small energy range of  $25 \pm 1.8$  keV, and thus only a small portion of the astrophysically relevant resonance region. Hence, their cross section is not suitable for stellar nucleosynthesis calculations without additional information.

The results from Heil *et al.* in 2008 [4] on the other hand were obtained by activation at 25 keV with a quasistellar neutron spectrum. Nevertheless, this cross section is significantly lower than our result for several reasons:

- (1) Reference cross section: We use the  $^{197}\text{Au}(n, \gamma)$  cross section published by [12] in 2014 as reference, which is 683 mb at 25 keV instead of the formerly used 648 mb from [23].
- (2) Quasistellar spectrum: The conversion of the activation cross section to the 25 keV stellar cross section was based on data from JEFF/3.1. But these evaluated cross section data show an energy dependence that is different from the measured one, resulting in a slight underestimation of the conversion factor.
- (3) Copper backing: We performed Monte Carlo simulations to estimate the effect of the choice of backing material, which included the geometry of the backing, gold monitors, and sample. The influence of the backing material was quantified by the relative numbers of activated nuclei of the sample and the monitors. We found significant effects in the case of sample and backing being of the same material. For the activation of [4] the Li layers were evaporated onto copper backings with a thickness of 1 mm. Due to the reduction of the neutron flux inside the backing the number of activated nuclei is reduced. The results of the simulations depend on the used evaluated data and

vary, e.g., between 13.7% for JENDL-4.0 and 10.9% for TENDL-2015. Figure 11 shows the effect on the neutron spectrum in the case of the TENDL-2015 data. For the case of a silver backing on the other hand we expect from our simulations only a marginal effect of  $\approx 0.2\%$ . However, a reliable correction factor for the renormalization of the data from [4] has to be determined experimentally.

## V. SUMMARY

The neutron capture cross section of  $^{63}\text{Cu}$  has been remeasured with a combination of the activation and TOF technique in the energy range from about 75 eV to 500 keV. By activation with a quasistellar neutron spectrum at JRC in Geel, Belgium, the stellar 25 keV cross section was determined to be

$$\langle \sigma \rangle_{25\text{keV}} = 92.12 \pm 1.19 \pm 6.35 \text{ mb.} \quad (7)$$

The energy dependency of the cross section was measured with an isotopically enriched  $^{63}\text{Cu}$  sample that was placed in the center of the DANCE detector array at LANSCE. The involved methods for data analysis allow the identification and subtraction of various types background, especially background from scattered neutrons former TOF experiments were often afflicted with. Using the activation cross section for the normalization of the differential cross section, the often difficult determination of the efficiency of the TOF data could be avoided. This way relatively low systematic uncertainties of 8.7% were achieved. Our results are in good agreement with the data from [8] and also with the evaluated cross sections from TENDL-2015. We provide Maxwellian-averaged cross sections for the whole temperature range relevant for different scenarios of the s-process nucleosynthesis.

## ACKNOWLEDGMENTS

This project was supported through the Nuclear Astrophysics Virtual Institute, Helmholtz Young Investigator project VH-NG-327, BMBF project 05P15RFFN1, HIC for FAIR, and has received funding from the European Research Council under the European Union's Seventh Framework Programme

(FP/2007-2013), ERC Grant Agreement No. 615126. This work benefited from the use of the LANSCE accelerator facility at Los Alamos National Laboratory. Work was performed under the auspices of the US Department of Energy

by Los Alamos National Security, LLC, under Contract No. DE-AC52-06NA25396. One of us (H.Y.L.) was supported by the US Department of Energy, Office of Science, Office of Nuclear Physics.

- 
- [1] F. Käppeler, R. Gallino, S. Bisterzo, and W. Aoki, *Rev. Mod. Phys.* **83**, 157 (2011).
- [2] M. Pignatari, R. Gallino, M. Heil, M. Wiescher, F. Käppeler, F. Herwig, and S. Bisterzo, *Astrophys. J.* **710**, 1557 (2010).
- [3] R. Reifarh, C. Lederer, and F. Käppeler, *J. Phys. G: Nucl. Part. Phys.* **41**, 053101 (2014).
- [4] M. Heil, R. Detwiler, R. E. Azuma, A. Couture, J. Daly, J. Görres, F. Käppeler, R. Reifarh, P. Tischhauser, C. Ugalde *et al.*, *Phys. Rev. C* **78**, 025803 (2008).
- [5] A. Arcones and F.-K. Thielemann, *J. Phys. G: Nucl. Part. Phys.* **40**, 013201 (2013).
- [6] B. Singh, *Nucl. Data Sheets* **78**, 395 (1996).
- [7] L.-S. The, M. F. El Eid, and B. S. Meyer, *Astrophys. J.* **655**, 1058 (2007).
- [8] M. Pandey, J. Garg, and J. Harvey, *Phys. Rev. C* **15**, 600 (1977).
- [9] R. Reifarh, T. Bredeweg, A. Alpizar-Vicente, J. Browne, E.-I. Esch, U. Greife, R. Haight, R. Hatarik, A. Kronenberg, J. O'Donnell *et al.*, *Nucl. Instrum. Methods Phys. Res., Sect. A* **531**, 530 (2004).
- [10] M. Heil, F. Käppeler, E. Uberseder, R. Gallino, and M. Pignatari, *Phys. Rev. C* **77**, 015808 (2008).
- [11] R. Reifarh, M. Heil, F. Käppeler, and R. Plag, *Nucl. Instrum. Methods Phys. Res., Sect. A* **608**, 139 (2009).
- [12] C. Massimi, B. Becker, E. Dupont, S. Kopecky, C. Lampoudis, R. Massarczyk, M. Moxon, V. Pronyaev, P. Schillebeeckx, I. Sirakov *et al.*, *Eur. Phys. J. A* **50**, 1 (2014).
- [13] B. Singh, *Nucl. Data Sheets* **108**, 197 (2007).
- [14] H. Xiaolong and K. Mengxiao, *Nucl. Data Sheets* **133**, 221 (2016).
- [15] E.-I. Esch, R. Reifarh, E. Bond, T. Bredeweg, A. Couture, S. Glover, U. Greife, R. Haight, A. Hatarik, R. Hatarik *et al.*, *Phys. Rev. C* **77**, 034309 (2008).
- [16] R. Reifarh, M. Heil, F. Käppeler, F. Voss, K. Wisshak, R. Haight, M. Dragowsky, M. Fowler, R. Rundberg, J. Ullmann *et al.*, Los Alamos National Laboratory Technical Report No. LA-UR-01-4185 2001 (unpublished).
- [17] M. Heil, R. Reifarh, M. M. Fowler, R. C. Haight, F. Käppeler, R. S. Rundberg, E. H. Seabury, J. L. Ullmann, J. B. Wilhelmy, and K. Wisshak, *Nucl. Instrum. Methods Phys. Res., Sect. A* **459**, 229 (2001).
- [18] J. Wouters, A. Vicente, T. Bredeweg, E. Esch, R. Haight, R. Hatarik, J. O'Donnell, R. Reifarh, R. Rundberg, J. Schwantes *et al.*, *IEEE Trans. Nucl. Sci.* **53**, 880 (2006).
- [19] M. Mocko and G. Muhrer, *Nucl. Instrum. Methods Phys. Res., Sect. A* **704**, 27 (2013).
- [20] Z. Bao, H. Beer, F. Käppeler, F. Voss, K. Wisshak, and T. Rauscher, *At. Data Nucl. Data Tables* **76**, 70 (2000).
- [21] I. Dillmann, M. Heil, F. Käppeler, R. Plag, T. Rauscher, and F. Thielemann, [arXiv:0805.4749](https://arxiv.org/abs/0805.4749).
- [22] H. Beer, F. Voss, and R. Winters, *Astrophys. J. Suppl. Ser.* **80**, 403 (1992).
- [23] W. Ratynski and F. Käppeler, *Phys. Rev. C* **37**, 595 (1988).